Neuron
Article

Bassoon and the Synaptic Ribbon Organize Ca^{2+} Channels and Vesicles to Add Release Sites and Promote Refilling

Thomas Frank,[1,2,3] Mark A. Rutherford,[1,10] Nicola Strenzke,[4,5,10] Andreas Neef,[3,10] Tina Pangršič,[1] Darina Khimich,[1] Anna Fejtova,[6] Eckart D. Gundelfinger,[6] M. Charles Liberman,[5] Benjamin Harke,[7] Keith E. Bryan,[8] Amy Lee,[8] Alexander Egner,[7] Dietmar Riedel,[9,*] and Tobias Moser[1,2,3,*]

[1]InnerEarLab, Department of Otolaryngology and Center for Molecular Physiology of the Brain, University of Göttingen Medical Center, 37099 Göttingen, Germany
[2]International Max Planck Research School for Neurosciences, Göttingen Graduate School for Neurosciences and Molecular Biosciences, 37077 Göttingen, Germany
[3]Bernstein Center for Computational Neuroscience, 37073 Göttingen, Germany
[4]Auditory Systems Physiology Group, Department of Otolaryngology and Center for Molecular Physiology of the Brain, University of Göttingen Medical Center, 37099 Göttingen, Germany
[5]Eaton Peabody Laboratory, Massachusetts Eye and Ear Infirmary, Boston, MA 02114, USA
[6]Department of Neurochemistry and Molecular Biology, Leibniz Institute for Neurobiology, 39118 Magdeburg, Germany
[7]Department of Nanobiophotonics, Max Planck Institute for Biophysical Chemistry, 37077 Göttingen, Germany
[8]Department of Molecular Physiology and Biophysics, University of Iowa, Iowa City, IA 52242, USA
[9]Laboratory of Electron Microscopy, Max Planck Institute for Biophysical Chemistry, 37077 Göttingen, Germany
[10]These authors contributed equally to the work
*Correspondence: driedel@gwdg.de (D.R.), tmoser@gwdg.de (T.M.)
DOI 10.1016/j.neuron.2010.10.027

SUMMARY

At the presynaptic active zone, Ca^{2+} influx triggers fusion of synaptic vesicles. It is not well understood how Ca^{2+} channel clustering and synaptic vesicle docking are organized. Here, we studied structure and function of hair cell ribbon synapses following genetic disruption of the presynaptic scaffold protein Bassoon. Mutant synapses—mostly lacking the ribbon—showed a reduction in membrane-proximal vesicles, with ribbonless synapses affected more than ribbon-occupied synapses. Ca^{2+} channels were also fewer at mutant synapses and appeared in abnormally shaped clusters. Ribbon absence reduced Ca^{2+} channel numbers at mutant and wild-type synapses. Fast and sustained exocytosis was reduced, notwithstanding normal coupling of the remaining Ca^{2+} channels to exocytosis. In vitro recordings revealed a slight impairment of vesicle replenishment. Mechanistic modeling of the in vivo data independently supported morphological and functional in vitro findings. We conclude that Bassoon and the ribbon (1) create a large number of release sites by organizing Ca^{2+} channels and vesicles, and (2) promote vesicle replenishment.

INTRODUCTION

Sensory encoding in the auditory and visual system of vertebrates relies on transformation of graded receptor potentials into rates of neurotransmitter release at ribbon synapses. The synaptic ribbon, an electron-dense structure anchored at the active zone, tethers a halo of synaptic vesicles (Glowatzki et al., 2008; Nouvian et al., 2006; Sterling and Matthews, 2005). Aside from its major component, RIBEYE (Khimich et al., 2005; Schmitz et al., 2000; Zenisek et al., 2004), the ribbon also contains scaffold proteins such as Bassoon and Piccolo (Dick et al., 2001; Khimich et al., 2005; tom Dieck et al., 2005). Genetic disruption of Bassoon perturbs the anchoring of ribbons to the active zones (AZs) of photoreceptors (Dick et al., 2003) and cochlear inner hair cells (IHCs) (Khimich et al., 2005). At the IHC synapse, where the functional effects of Bassoon disruption and ribbon loss are best studied, fast exocytosis is reduced (Khimich et al., 2005), and sound encoding by the postsynaptic spiral ganglion neurons impaired (Buran et al., 2010). Moreover, IHCs of these Bassoon mouse mutants ($Bsn^{\Delta Ex4/5}$) show smaller Ca^{2+} currents. However, matching Ca^{2+} currents by reducing the driving force for Ca^{2+} in wild-type IHCs does not equalize fast exocytosis between wild-type and mutant IHCs. This, together with an unaltered rate constant of fast exocytosis in mutant IHCs—indicating a normal vesicular release probability—led to the previous hypothesis that the defect primarily reflects a reduction of the readily releasable pool of vesicles (RRP) due to the loss of the ribbon (Khimich et al., 2005).

However, the exact structural and functional correlates of the RRP reduction remained unclear. For example, potential differences between mutant AZs that still have a ribbon (ribbon-occupied) and their ribbonless counterparts have not yet been investigated. Moreover, it is not known to which degree and by which mechanism Ca^{2+} influx is affected at the level of individual synapses and how this might contribute to the exocytic deficit. Several mechanisms may explain the impairment of fast exocytosis in IHCs of $Bsn^{\Delta Ex4/5}$ mutants. First, mutant AZs may contain

fewer vesicular docking sites and/or closely colocalized Ca^{2+} channels. Together, they have been suggested to constitute the numerous release sites of the IHC AZ at which vesicle fusion is controlled by the Ca^{2+} nanodomain of one or few nearby active Ca^{2+} channels (Brandt et al., 2005; Moser et al., 2006; Goutman and Glowatzki, 2007). Vesicles docked and primed in these "slots" probably constitute the RRP, of which the released fraction but not the release kinetics depends on the number of slots recruited by a given stimulus (Brandt et al., 2005; Furukawa and Matsuura, 1978; Wittig and Parsons, 2008). Therefore, fewer release sites, because of fewer Ca^{2+} channels (Neef et al., 2009) and/or fewer docking sites, could explain impaired fast exocytosis as a deficit of RRP size. Second, even if the number of release sites was unchanged, the standing RRP would be diminished if vesicle occupancy at each of these sites was reduced in $Bsn^{\Delta Ex4/5}$ IHCs, e.g., because of impaired replenishment or enhanced undocking of vesicles. Third, the coupling between Ca^{2+} influx and Ca^{2+} sensors of the exocytosis machinery could be altered, such that not all vesicles can contribute to fast exocytosis, even after proper docking and biochemical priming. This point subsumes changes in diffusion, buffering, or homeostasis of $[Ca^{2+}]_i$, as well as an increased distance between channels and Ca^{2+} sensors, positional priming (Neher and Sakaba, 2008), as it was reported at the *Drosophila* neuromuscular junction after disruption of the presynaptic scaffold protein Bruchpilot (Kittel et al., 2006). Finally, the intrinsic Ca^{2+} sensitivity of exocytosis could be altered.

The availability of a number of techniques such as improved stimulated emission depletion (STED) microscopy and fast confocal imaging of Ca^{2+} influx, as well as the generation of another Bassoon-deficient mouse line (Bsn^{gt}) now allowed us to address these questions. Here, we used in vitro and in vivo physiology in combination with light and electron microscopy and computational modeling to study in detail structural and functional effects of Bassoon disruption at both ribbon-occupied and ribbonless AZs. Our results indicate that both functional inactivation of Bassoon and ribbon loss reduce the number of presynaptic Ca^{2+} channels. Membrane tethering of vesicles was improved but not fully normal at ribbon-occupied mutant AZs, suggesting a partial function of these ribbons. Mutant IHCs showed a reduction in the number of release sites while maintaining an intact coupling of Ca^{2+} influx to exocytosis. Vesicle replenishment was slightly impaired in in vitro experiments. We conclude that the multiprotein complex of the synaptic ribbon and Bassoon organize Ca^{2+} channels and synaptic vesicles at the AZ, thereby creating a large number of release sites.

RESULTS

The most prominent morphological phenotype of IHCs associated with the disruption of Bassoon function in mouse mutants with partial gene deletion ($Bsn^{\Delta Ex4/5}$) is the loss of synaptic ribbons from their AZs (Buran et al., 2010; Khimich et al., 2005). In IHCs of immunolabeled whole-mounted organs of Corti from 3-week-old mice, we used confocal microscopy to count ribbon synapses as juxtaposed spots of presynaptic CtBP2/RIBEYE (labeling ribbons) and postsynaptic GluR2/3 (labeling glutamate receptor clusters). Per IHC in $Bsn^{\Delta Ex4/5}$, we found on average 2.5 ribbon-occupied synapses (22% of 1240 synapses, n = 112 IHCs) instead of 11.9 ribbon-occupied synapses in Bsn^{wt} (97% of 1028 synapses, n = 84 IHCs). Consistent with observations at retinal photoreceptor ribbon synapses (Dick et al., 2003), we detected expression of the N-terminal Bassoon fragment in IHCs of $Bsn^{\Delta Ex4/5}$ mice (Figure S1A, available online) but found that it was not localized to afferent IHC synapses, arguing against a residual function at the AZ. This observation and the absence of an auditory deficit in 8-week-old heterozygous $Bsn^{\Delta Ex4/5}$ mice (data not shown) do not support the idea of a dominant negative effect of the N-terminal Bassoon fragment. We also observed fewer ribbon-occupied synapses in IHCs of the newly generated Bassoon-deficient mouse line Bsn^{gt} (4.8 versus 9.6 ribbon-occupied synapses per IHC in wild-type), which, like $Bsn^{\Delta Ex4/5}$ mice, showed a mild hearing impairment (threshold increase by 23 dB for click stimuli in four Bsn^{gt} mice compared to three wild-type littermates versus 37 dB increase in $Bsn^{\Delta Ex4/5}$; Pauli-Magnus et al., 2007). A weak Bassoon immunolabeling was observed at a small subset (approximately 10%) of synapses in Bsn^{gt} IHCs (Figure S1B), potentially explaining the higher number of ribbon-occupied AZs in Bsn^{gt} IHCs.

Reduction of Membrane-Proximal Vesicles at Hair Cell Synapses of Bassoon Mutants

We studied effects of Bassoon disruption and ribbon loss on synaptic ultrastructure in electron micrographs of 80 nm sections (Figures 1A and 1B). Membrane-proximal vesicles at apparently ribbonless $Bsn^{\Delta Ex4/5}$ AZs showed an altered distribution. When measuring their lateral position relative to the presynaptically projected center of the postsynaptic density, we observed a broad and seemingly random distribution of those vesicles at the AZ (Figure 1C, gray bars). In contrast, membrane-proximal vesicles at AZs of Bsn^{wt} IHCs fell into two categories: ribbon-associated (red open bars) and non-ribbon-associated (black open bars). The latter population was indistinguishable from membrane-proximal vesicles at ribbonless $Bsn^{\Delta Ex4/5}$ AZs ($p = 0.27$, Kolmogorov-Smirnov test). We then counted the total number of those vesicles in single 80 nm sections and observed significantly fewer vesicles at apparently ribbonless (1.5 ± 0.2 vesicles/AZ section, 53 AZs) and ribbon-occupied $Bsn^{\Delta Ex4/5}$ synapses (2.0 ± 0.4 vesicles/AZ section, 10 AZs) than at ribbon-occupied Bsn^{wt} synapses (4.2 ± 0.4 vesicles/AZ section, 26 AZs, $p < 0.01$ for both comparisons).

Because the absence of a synaptic ribbon cannot unequivocally be concluded from not seeing a ribbon in a single 80 nm synaptic section, we used electron tomography to address potential differences between ribbon-occupied and ribbonless AZs in *Bsn* mutant mice (Figures 1E–1H). We used Bsn^{gt} mice for these experiments because of their larger fraction of ribbon-occupied AZs. In electron tomography, we counted vesicles that were tethered to the plasma membrane by filamentous linkers (see Figure 1D for examples; Fernández-Busnadiego et al., 2010). Indeed, we found a trend toward more membrane-tethered vesicles when a ribbon was present (6.4 ± 0.8, n = 10 at ribbon-occupied Bsn^{gt} AZs versus 3.7 ± 1.1, n = 6 at ribbonless Bsn^{gt} AZs; $p = 0.1$), probably reflecting the addition of a ribbon-associated vesicle population. As in the analysis of 80 nm sections of $Bsn^{\Delta Ex4/5}$ AZs, vesicle numbers at ribbon-occupied

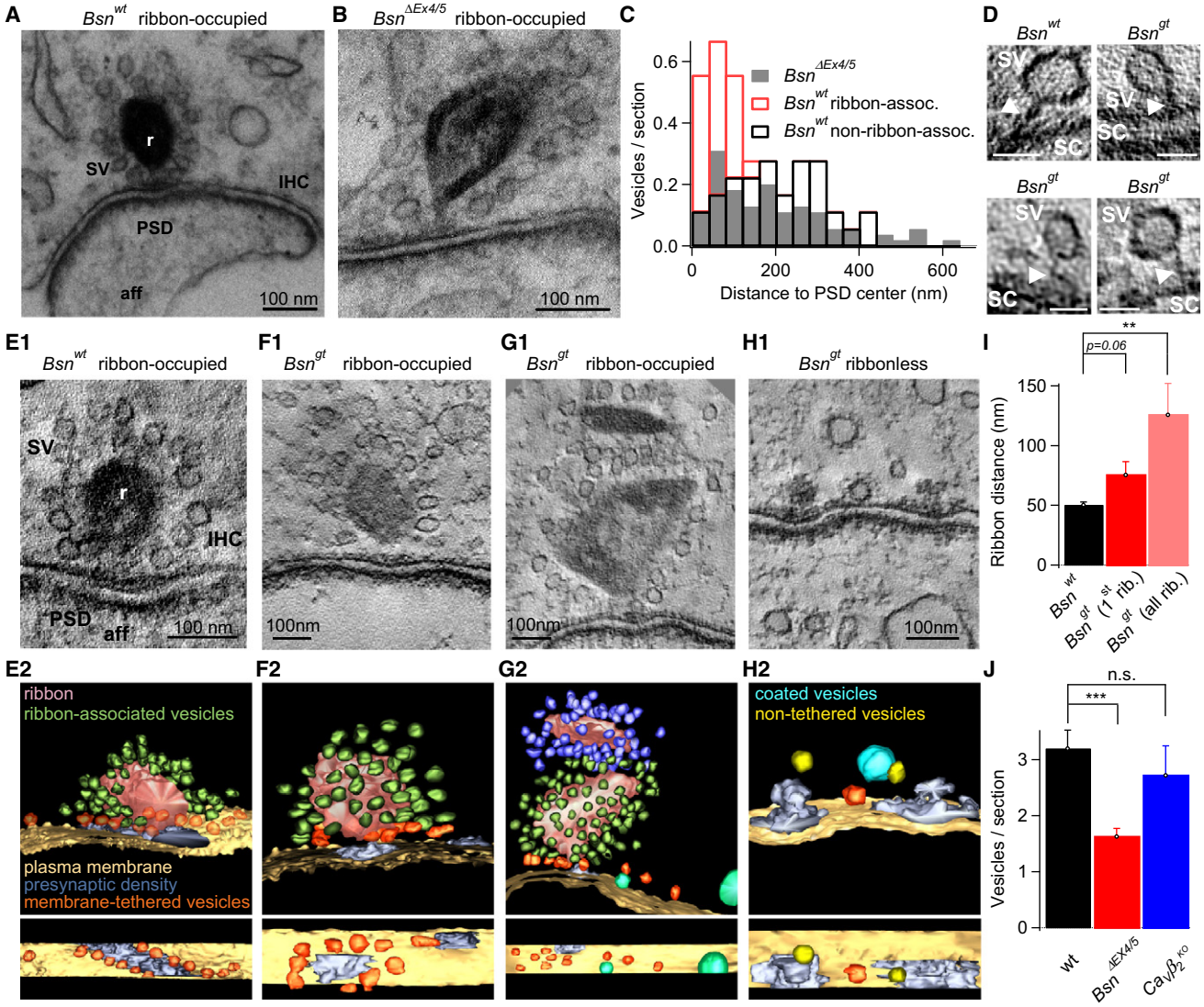

Figure 1. Synaptic Ultrastructure and Vesicle Distribution in the Presence and Absence of the Synaptic Ribbon

(A and B) Electron micrographs of single thin sections of Bsn^{wt} (A) and $Bsn^{\Delta Ex4/5}$ ribbon-occupied IHC ribbon synapses (B). The following abbreviations are used: r, ribbon; SV, synaptic vesicle; PSD, postsynaptic density; aff, afferent bouton.

(C) Distribution of membrane-proximal synaptic vesicles in Bsn^{wt} and $Bsn^{\Delta Ex4/5}$ IHCs as a function of distance from the PSD center. The histogram was normalized to the number of sections analyzed in the respective genotype (Bsn^{wt}, n = 58 SVs, 18 sections; $Bsn^{\Delta Ex4/5}$, n = 74 SVs, 36 sections).

(D) Example slices from single-axis electron tomograms showing membrane-tethered synaptic vesicles. Tethers are marked by arrowheads. SC denotes synaptic cleft. The scale bars represent 40 nm.

(E–H) Single slices from tomograms for Bsn^{wt} (E1), Bsn^{gt} ribbon-occupied (F1 and G1), and Bsn^{gt} ribbonless synapses (H1). (E2–H2, upper) Tomogram-based model of Bsn^{wt} (E2), Bsn^{gt} ribbon-occupied (F2 and G2), and Bsn^{gt} ribbonless synapses (H2). Vesicles distant from the ribbon and the plasma membrane are not shown. (Lower) Same models as in upper but only showing membrane-tethered (orange) SVs used for analysis (see Results).

(I) Bar plot showing mean minimal distance between ribbon and plasma membrane as measured in electron tomograms of Bsn^{wt} AZs (black; n = 5 ribbons/5 AZs), of just the proximal ribbons at Bsn^{gt} AZs (red; n = 10 ribbons/10 AZs), and of all ribbons at Bsn^{gt} AZs (light red; n = 16 ribbons/10 AZs). The error bars represent standard error of the mean (SEM).

(J) Bar plot showing average number of membrane-proximal SVs per thin section for wild-type (black; n = 46 AZs, pooled data from *Bsn* and $Ca_V\beta_2$ wild-type littermates) and mutant synapses. $Bsn^{\Delta Ex4/5}$ (red; n = 67 AZs), but not $Ca_V\beta_2$ knockout synapses (blue; n = 32 AZs), had approximately one-half the numbers of membrane-proximal SVs. The error bars represent SEM.

Bsn^{gt} AZs did not reach Bsn^{wt} levels (10.6 ± 0.7, n = 5, $p < 0.01$). We also observed that, unlike at Bsn^{wt} synapses, ribbons of Bsn^{gt} tended to be farther away from the plasma membrane (Figure 1I). In fact, we found a spectrum of ribbon-anchorage phenotypes: from wild-type-like proximity to loosely anchored ribbons (often accompanied by a second detached ribbon) to complete ribbon absence. It is tempting to speculate that loosely anchored ribbons may not fully promote membrane tethering of vesicles.

We note that even in the 250 nm tissue sections that were used for tomography, the reported vesicle numbers represent underestimates of the full complement of membrane-proximal vesicles because synapses were not completely included along one dimension. However, this error equally affected each synapse type, and tomograms fully contained the synapse in the other two dimensions. Notably, we found that the electron-dense material lining the presynaptic plasma membrane (presynaptic density) was longer and thicker at ribbon-occupied Bsn^{wt} AZs than the spot-like presynaptic densities at Bsn^{gt} AZs (regardless of ribbon presence; Figures 1E2–1H2 and Table S1), which sometimes harbored more than one density (Figures 1F2 and1 H2).

Finally, we also studied AZs in IHCs of mouse mutants that contain fewer Ca^{2+} channels because of a lack of the β_2 subunit ($Ca_V\beta_2$; Neef et al., 2009). $Ca_V\beta_2$-deficient IHCs display a 70% reduction of both Ca^{2+} influx and RRP exocytosis despite the presence of synaptic ribbons. Number (Figure 1J, data from wild-type littermates of $Bsn^{\Delta Ex4/5}$ and $Ca_V\beta_2$ mutants were pooled) and distribution (data not shown) of membrane-proximal vesicles were unaltered in 80 nm sections, suggesting that proteins of the macromolecular ribbon complex, but not Ca^{2+} channels, are required for the formation of vesicle docking sites.

Fewer Ca^{2+} Channels and Altered Shape of Ca^{2+} Channel Clusters

Voltage-gated Ca^{2+} influx is decreased in IHCs of *Bsn* mutants ($Bsn^{\Delta Ex4/5}$; Khimich et al., 2005). Here, we explored changes of presynaptic Ca^{2+} signaling by morphological and functional imaging. First, we studied presynaptic Ca^{2+} channel clusters by confocal and STED microscopy following immunolabeling of $Ca_V1.3$ Ca^{2+} channels. Images of $Bsn^{\Delta Ex4/5}$ and Bsn^{wt} organs of Corti that had been processed for immunohistochemistry in parallel and following the same protocol were acquired with identical microscope settings and analyzed for intensity and shape of $Ca_V1.3$ immunofluorescent spots (Figure 2). We estimated the short and long axes of the elliptic fluorescent objects by fitting 2D Gaussian functions to the background-subtracted images (see Supplemental Experimental Procedures). The fluorescence integral within this region served as a proxy of the abundance of presynaptic Ca^{2+} channels. In Bsn^{wt} organs of Corti, the synaptic location of $Ca_V1.3$ clusters (Figure 2A) was readily confirmed by the colocalization with synaptic ribbons (Brandt et al., 2005; Meyer et al., 2009) and Bassoon (Figure S1B). In addition, some lower intensity spot-like immunofluorescence was present in IHCs (Figure 2). In $Bsn^{\Delta Ex4/5}$ and Bsn^{wt} IHCs, the synaptic localization of Ca^{2+} channel clusters was identified by costaining for postsynaptic glutamate receptors (GluR2; Figure S1C). This confirmed that Ca^{2+} channels remained clustered at synapses despite both the disruption of Bassoon and, in most cases, absence of the ribbon. In comparison to Bsn^{wt}, the immunofluorescence of $Ca_V1.3$ clusters colocalized with GluR2 was reduced at $Bsn^{\Delta Ex4/5}$ synapses (Figure 2B and Figure S1D).

In experiments colabeling for $Ca_V1.3$ and the synaptic ribbon marker RIBEYE/CtBP2, we were able to separate ribbon-occupied AZs from ribbonless AZs in $Bsn^{\Delta Ex4/5}$ and Bsn^{wt} mice. Because of the absence of an additional synaptic marker at ribbonless $Bsn^{\Delta Ex4/5}$ AZs, and to exclude nonsynaptic $Ca_V1.3$ immunofluorescent spots from analysis, we considered only the ten brightest spots in each cell for both genotypes. This approach was justified by knowledge of cochlear location (ten synapses per cell in apical turn; Meyer et al., 2009) and the observation that 92.2% and 89.4% of the ten brightest Ca^{2+} channel clusters were juxtaposed to GluR2 immunofluorescent spots in $Bsn^{\Delta Ex4/5}$ and Bsn^{wt} IHCs, respectively. In confocal images, $Ca_V1.3$ immunofluorescence was reduced by 42% at $Bsn^{\Delta Ex4/5}$ AZs (Figure 2B; $p < 1e{-}20$). As quantified in Figures 2B and 2C and Table 1, the $Ca_V1.3$ immunofluorescence decreased in the order: ribbon-occupied Bsn^{wt} > ribbonless Bsn^{wt} > ribbon-occupied $Bsn^{\Delta Ex4/5}$ > ribbonless $Bsn^{\Delta Ex4/5}$. $Ca_V1.3$ channel clusters of ribbon-occupied $Bsn^{\Delta Ex4/5}$ AZs were also more similar to Bsn^{wt} AZs in shape than those of ribbonless $Bsn^{\Delta Ex4/5}$ AZs. The altered shape of the latter was evident in a smaller long-to-short axis ratio (standard STED; Figures 2D and 2E and Table 1).

To resolve a potential substructure within $Ca_V1.3$ clusters, we used a custom-built STED microscope (STED*; lateral point spread function [PSF] less than 100 nm at a tissue depth of 15 to 25 μm; yellow range in Figure 2E). Ca^{2+} channel clusters of Bsn^{wt} AZs typically displayed one to three stripes of $Ca_V1.3$ immunofluorescence (Figure 2F). Parallel confocal observation of the associated CtBP2/RIBEYE immunofluorescence suggested that these synapses featured one ribbon regardless of the number of stripes, although two closely-spaced ribbons may fall within the confocal PSF and thus may not be resolved as individual ribbons. In contrast, $Bsn^{\Delta Ex4/5}$ AZs showed $Ca_V1.3$ immunofluorescence spots rather than stripes (Figure 2F; full width at half maximum of long and short axes: 120 ± 7.9 nm and 95 ± 5.5 nm, n = 13) with ribbon-occupied AZs typically harboring more spots than ribbonless AZs. $Ca_V1.3$ immunofluorescent stripes and spots were reminiscent of the patterns of presynaptic density observed in electron tomography (Figures 1E2–1H2). In summary, the abundance of presynaptic Ca^{2+} channels and the cluster shape are altered upon Bassoon disruption, which might reflect the loss of a direct Bassoon action on Ca^{2+} channel clustering or of the Bassoon-mediated ribbon anchorage. To test for a potential role of Bassoon in the direct presynaptic anchoring of Ca^{2+} channels, we determined whether Bassoon and the $Ca_V1.3$ channel interacted in a heterologous expression system. We did not find evidence that Bassoon coimmunoprecipitated or colocalized with $Ca_V1.3$ in transfected HEK293T cells (Figure S4). Therefore, the role of Bassoon in recruiting Ca^{2+} channels to the AZ may not involve a direct association of the two proteins.

Reduced Synaptic Ca^{2+} Influx Results from Fewer Channels and Lower Open Probability

To study synaptic Ca^{2+} influx in $Bsn^{\Delta Ex4/5}$ IHCs, we performed whole-cell patch-clamp recordings of Ca^{2+} current (I_{Ca}) and confocal imaging of presynaptic Ca^{2+} microdomains (Frank et al., 2009). We found a reduction of peak whole-cell I_{Ca} amplitude in $Bsn^{\Delta Ex4/5}$ IHCs of 3-week-old mice (Figure 3, Table 1, Figure S2, and Table S1). It ranged between 62% (ruptured-patch, 5 mM $[Ca^{2+}]_e$; Figure 3A and Table 1) and 69% (perforated-patch, 10 mM $[Ca^{2+}]_e$; Figure S2 and Table S1) of Bsn^{wt} amplitude. The

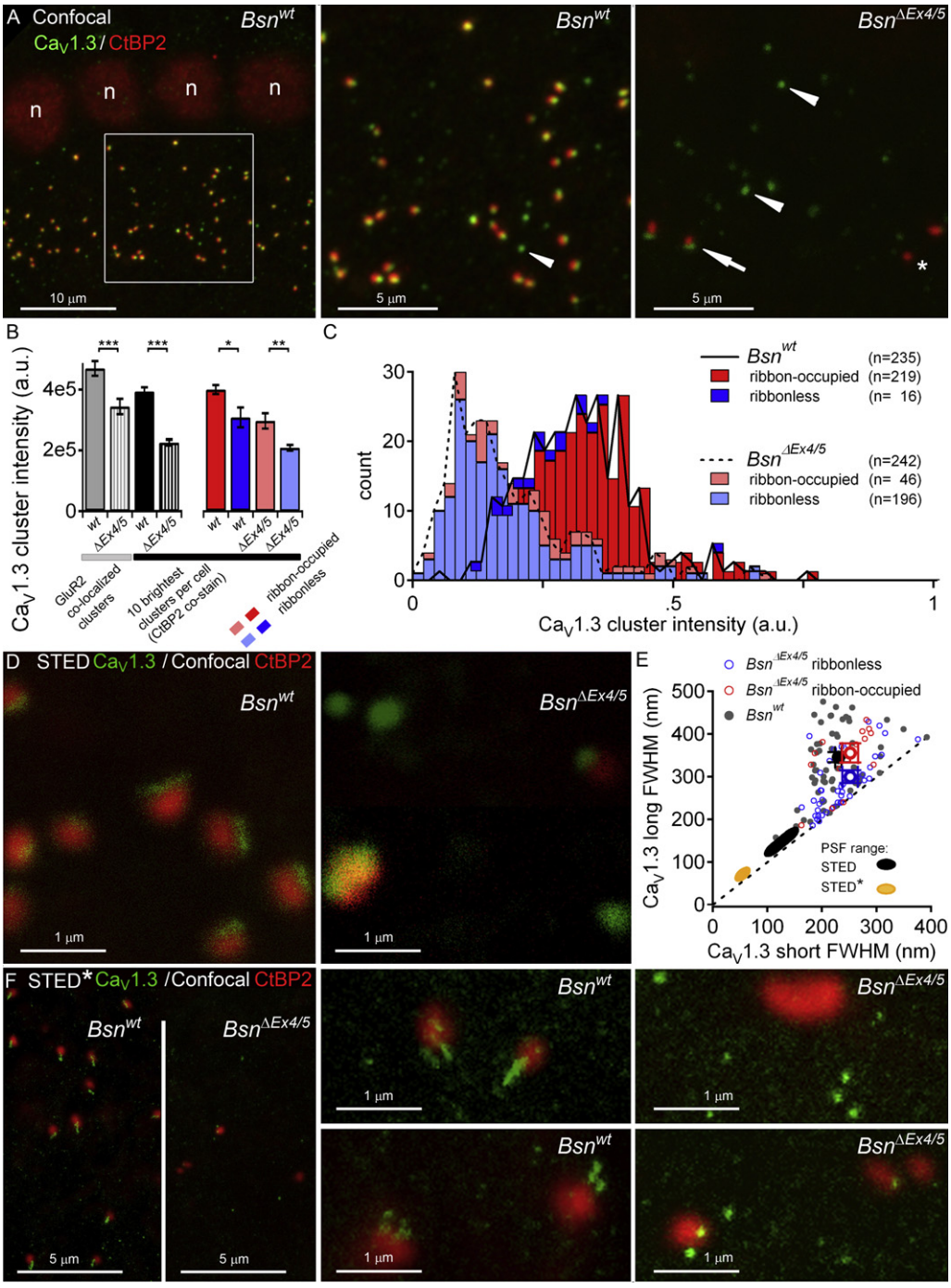

Figure 2. Decreased Immunofluorescence and Altered Shape of $Ca_V1.3$ Clusters

(A) Projections of confocal sections of IHCs of apical cochlear coils immunolabeled for synaptic ribbons (CtBP2, red) and Ca^{2+} channels ($Ca_V1.3$, green) as used for analysis in (B and C). (Left) Four Bsn^{wt} IHCs (n is an abbreviation for nuclei). (Middle) Enlargement of part of the synaptic layer (white box, left) showing colocalization of CtBP2 and $Ca_V1.3$. (Right) In the partial gene deletion mutant ($Bsn^{\Delta Ex4/5}$), Ca^{2+} channels still cluster but few ribbons remain (P28). Arrowheads point to ribbonless $Ca_V1.3$ clusters in wild-type and mutant. Arrow points to a ribbon-occupied $Ca_V1.3$ cluster. Asterisk labels a floating ribbon.

(B) $Ca_V1.3$ immunofluorescence intensity (mean ± SEM, a.u.) was less at $Bsn^{\Delta Ex4/5}$ synapses when analyzing only $Ca_V1.3$ clusters that colocalized with GluR2 (gray; $Bsn^{\Delta Ex4/5}$ versus Bsn^{wt}, $p < 0.0005$) or when counting the ten brightest clusters per hair cell (black; $Bsn^{\Delta Ex4/5}$ versus Bsn^{wt}, $p < 1e^{-20}$). In both Bsn^{wt} and $Bsn^{\Delta Ex4/5}$, the presence of a ribbon (CtBP2 colocalized: ribbon occupied, red) was associated with greater $Ca_V1.3$ intensity when compared to ribbonless synapses (blue). Bsn^{wt} ribbon occupied versus Bsn^{wt} ribbonless, $p < 0.05$; $Bsn^{\Delta Ex4/5}$ ribbon occupied versus $Bsn^{\Delta Ex4/5}$ ribbonless, $p < 0.005$).

(C) $Ca_V1.3$ cluster intensity histogram for Bsn^{wt} (solid line) and $Bsn^{\Delta Ex4/5}$ (dotted line). Each distribution is decomposed into ribbon-occupied (red) and ribbonless (blue) clusters.

Table 1. Summary of IHC Physiology in *Bsn* Wild-Type and Mutant Mice

Parameter	Bsn^{wt}		$Bsn^{\Delta Ex4/5}$		p Value
$Ca_V1.3$ Immunofluorescence					
Intensity, confocal (a.u.)	Ribbonless: 3.1e5 ± 3e4 (n = 16)	Ribbon-occupied: 4.0e5 ± 1e4 (n = 219)	Ribbonless: 2.1e5 ± 1e4 (n = 196)	Ribbon-occupied: 2.9e5 ± 3e4 (n = 46)	Bsn^{wt}, ribbonless versus ribbon-occupied, $p < 0.05$; $Bsn^{\Delta Ex4/5}$, ribbonless versus ribbon-occupied, $p < 0.01$; Bsn^{wt} versus $Bsn^{dEX4/5}$, $p < 0.001$
FWHM, STED, long:short (nm)		Ribbon-occupied: 345.9 ± 12: 230.0 ± 6 (n = 68)	Ribbonless: 300.3 ± 15: 251.4 ± 14 (n = 45)	Ribbon-occupied: 355.6 ± 22: 251.8 ± 15 (n = 16)	Bsn^{wt} versus $Bsn^{\Delta Ex4/5}$, ribbonless, $p < 0.001$; Bsn^{wt} versus $Bsn^{\Delta Ex4/5}$, ribbon-occupied, n.s.; $Bsn^{\Delta Ex4/5}$, ribbonless versus ribbon-occupied, $p < 0.05$
Whole-Cell Ca^{2+} Current					
Peak I_{Ca} (pA): 5 Ca^{2+}/−BayK	−179.5 ± 9.6 (N = 31)		−111.1 ± 6.2 (N = 38)		$p < 0.001$ (W)
Peak I_{Ca} (pA): 10 Ca^{2+}/+BayK	−417.5 ± 29.0 (N = 29)		−321.0 ± 33.9 (N = 19)		$p < 0.05$ (W)
N_{Ca}: 10 Ca^{2+}/+BayK	1574 ± 92 (N = 27)		1227 ± 111 (N = 22)		$p < 0.01$ (W)
Presynaptic Ca^{2+} Microdomains					
ΔF_{avg} (a.u.): 5 Ca^{2+}/−BayK	85.5 ± 9.1 (n = 74/N = 30)		30.5 ± 2.0 (n = 112/N = 45)		$p < 0.001$ (W)
ΔF_{avg} (a.u.): 5 Ca^{2+}/+BayK	89.5 ± 9.0 (n = 53/N = 21)		46.9 ± 5.2 (n = 52/N = 20)		$p < 0.001$ (W)
ΔF_{avg} (a.u.): ±BayK	$p = 0.14$ (W)		$p < 0.01$ (W)		
Exocytosis					
$\Delta C_{m,20\ ms}$(fF) − pp	13.2 ± 1.1 (N = 38)		7.9 ± 0.9 (N = 37)		$p < 0.001$ (W)
$Q_{Ca,20ms}$ (pC) − pp	4.4 ± 0.3 (N = 38)		3.0 ± 0.2 (N = 37)		$p < 0.001$ (W)
$\Delta C_{m,20\ ms}$(fF) − rp	8.1 ± 1.0 (N = 17)		4.7 ± 0.8 (N = 16)		$p < 0.01$ (W)
$Q_{Ca,20ms}$ (pC) − rp	3.3 ± 0.2 (N = 17)		2.6 ± 0.1 (N = 16)		$p < 0.05$ (T)
$\Delta C_{m,100\ ms}$ (fF) − pp	39.6 ± 5.2 (N = 41)		21.9 ± 4.3 (N = 40)		$p < 0.001$ (W)
$Q_{Ca,100ms}$ (pC) − pp	20.4 ± 1.4 (N = 41)		13.2 ± 0.9 (N = 40)		$p < 0.001$ (W)
$\Delta C_{m,100\ ms}$ (fF) − rp	35.1 ± 5.3 (N = 13)		19.5 ± 5.8 (N = 11)		$p < 0.01$ (W)
$Q_{Ca,100ms}$ (pC) − rp	15.5 ± 1.0 (N = 13)		11.2 ± 0.9 (N = 11)		$p < 0.01$ (T)
Sustained ΔC_m ($\Delta C_{m,100}$ − $\Delta C_{m,20}$; fF) −pp	26.8 ± 4.6 (N = 38)		15.1 ± 4.4 (N = 35)		$p < 0.001$ (W)

n denotes number of synapses ($Ca_V1.3$ immunofluorescence and presynaptic Ca^{2+} microdomains) and N number of IHCs (whole-cell Ca^{2+} current, Ca^{2+} imaging, and capacitance measurements). n.s. denotes not significant. For immunofluorescence, *Bsn* mutant data were separated into ribbonless and ribbon-occupied synapses. Statistical comparisons were made with an independent two-sample t test (T) or a Mann-Whitney-Wilcoxon (W) test (Experimental Procedures). The following abbreviations are used: a.u., arbitrary units; FWHM, full width at half-maximum; I_{Ca}, whole-cell Ca^{2+} current; N_{Ca}, number of Ca^{2+} channels; ΔF_{avg}, average Ca^{2+} microdomain amplitude; ΔC_m, exocytic membrane capacitance changes; pp, perforated-patch configuration; Q_{Ca}, Ca^{2+} current integral; rp, ruptured-patch configuration. Sustained ΔC_m was calculated cell-wise by subtracting the average ΔC_m response to 20 ms from the average ΔC_m response to 100 ms long depolarization. Data are presented as mean ± SEM.

difference from Bsn^{wt} was alleviated in the presence of the dihydropyridine agonist BayK8644 (77%, ruptured-patch, 10 mM $[Ca^{2+}]_e$; Figure 3B and Table 1), suggesting that Ca^{2+} channel open probability is reduced in $Bsn^{\Delta Ex4/5}$ IHCs in the absence of BayK8644. Moreover, we found that Ca^{2+} current activation was slowed in $Bsn^{\Delta Ex4/5}$ IHCs (Figure 3C and Figure S2), while it was indistinguishable from wild-type IHCs in the presence of BayK8644 (Figure 3D). Finally, the Ca^{2+} currents inactivated slightly more in $Bsn^{\Delta Ex4/5}$ IHCs (Figure 3E and Table S1).

To test whether the observed reduction in I_{Ca} was caused by changes in channel number (N_{Ca}), unitary current (i_{Ca}), or open probability (p_{open}), we performed a nonstationary fluctuation analysis on Ca^{2+} tail-currents ($[BayK8644]_e$ = 5 μM; Brandt et al., 2005). In line with the observed reduction in I_{Ca} amplitude,

(D) Single optical sections of CtBP2 (confocal) and $Ca_V1.3$ (standard STED) for size analysis in (E) of $Ca_V1.3$ clusters at Bsn^{wt} (left) and $Bsn^{\Delta Ex4/5}$ AZs (right).
(E) Compared to Bsn^{wt} (filled circles: individuals, gray; mean, black) and ribbon-occupied $Bsn^{\Delta Ex4/5}$ synapses (red open circles; mean, dark red), the ribbonless $Ca_V1.3$ clusters (blue open circles; mean, dark blue) fell closer to unity (dashed line). Apparent sizes of 40 nm beads mounted above and below the organ of Corti illustrate the PSF range for the two STED microscopes (black, Leica STED; yellow, custom STED*). The error bars represent SEM.
(F) STED* microscopy revealed ribbon-occupied Bsn^{wt} $Ca_V1.3$ clusters as one or more elongated stripes, not observed at $Bsn^{\Delta Ex4/5}$ synapses.

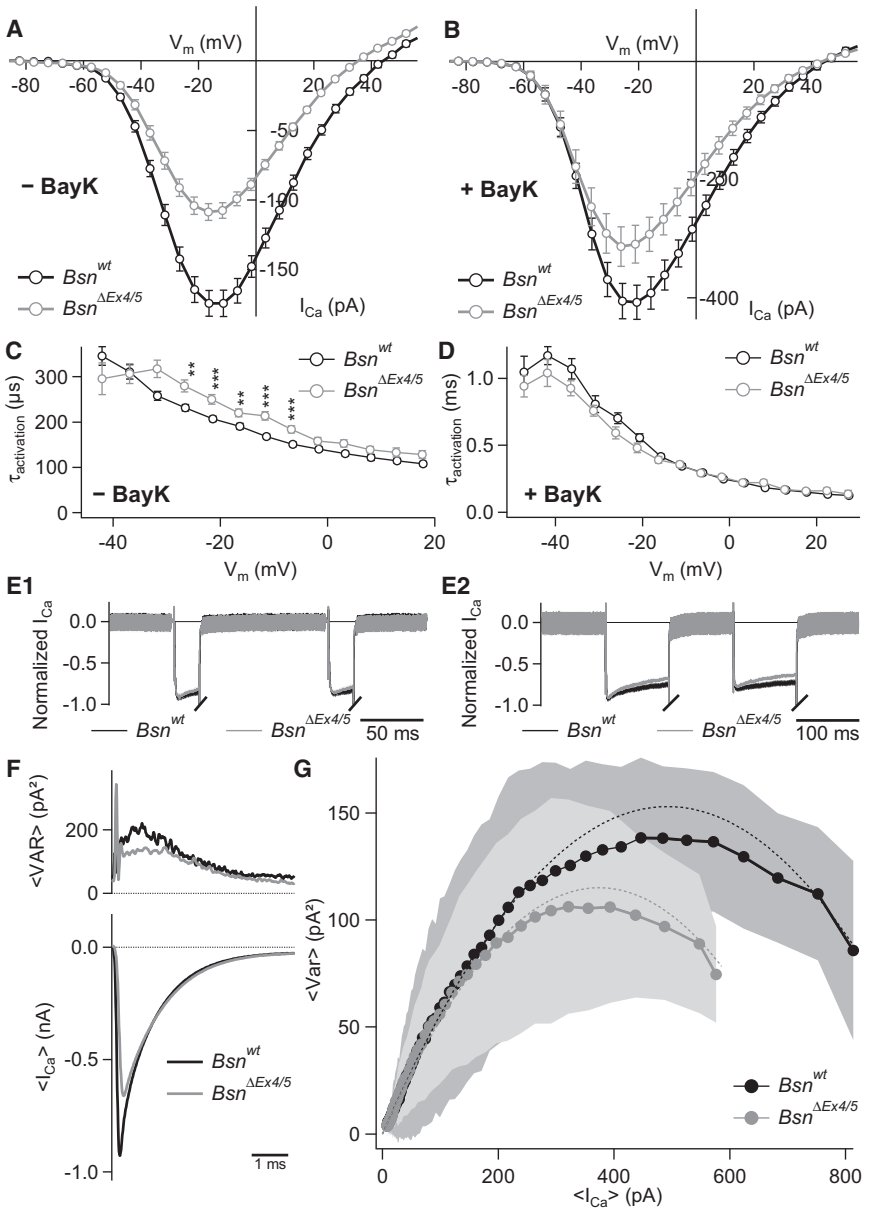

Figure 3. Biophysical Properties of Voltage-Dependent Whole-Cell Ca^{2+} Current (I_{Ca})

(A) Average steady-state I_{Ca}-V for Bsn^{wt} and $Bsn^{\Delta Ex4/5}$ IHCs in 5 mM $[Ca^{2+}]_e$ (n [Bsn^{wt}] = 31 IHCs, n [$Bsn^{\Delta Ex4/5}$] = 38 IHCs). Note the reduction of max. I_{Ca} to ~60% of wild-type level in $Bsn^{\Delta Ex4/5}$ IHCs (Table 1).

(B) As in (A) but in 10 mM $[Ca^{2+}]_e$ and presence of 5 μM BayK8644 (n [Bsn^{wt}] = 29 IHCs, n [$Bsn^{\Delta Ex4/5}$] = 19 IHCs). Note the smaller difference in max. I_{Ca} between the two genotypes ($Bsn^{\Delta Ex4/5}$: ~80% of Bsn^{wt} level; Table 1).

(C) Average time-constant of I_{Ca} activation in 5 mM $[Ca^{2+}]_e$ as a function of membrane voltage (V_m), derived from single exponential fits to the initial 3.5 ms of I_{Ca} (see Supplemental Experimental Procedures; n [Bsn^{wt}]: ≤ 30 IHCs, n [$Bsn^{\Delta Ex4/5}$]: ≤ 35 IHCs). Asterisks indicate V_m at which differences between genotypes were statistically significant (α = 0.05; Bonferroni correction). Average series resistance (R_S) was 6.0 ± 2.3 MΩ for Bsn^{wt} IHCs, and 6.1 ± 2.3 MΩ for $Bsn^{\Delta Ex4/5}$ IHCs (mean ± SD), respectively.

(D) Same as (C) but in 10 mM $[Ca^{2+}]_e$ and 5 μM extracellular BayK8644 (n [Bsn^{wt}]: ≤ 29 IHCs, n [$Bsn^{\Delta Ex4/5}$]: ≤ 19 IHCs). Average R_S was 4.7 ± 3.1 MΩ for Bsn^{wt} IHCs, and 5.3 ± 3.3 MΩ for $Bsn^{\Delta Ex4/5}$ IHCs (mean ± SD), respectively.

The error bars in (A–D) represent SEM.

(E1and E2) Average paired-pulse I_{Ca} traces (depolarization to V_m of maximum I_{Ca}; $[Ca^{2+}]_e$ = 10 mM) illustrate stronger inactivation in $Bsn^{\Delta Ex4/5}$ IHCs, being more evident for longer (100 ms; E2) than for shorter depolarizations (20 ms; E1).

(F) Example mean Ca^{2+} tail-currents (lower) used for nonstationary fluctuation analysis (Table 1 and Table S1), elicited by repolarizing IHCs from +57 mV to −68 mV, and corresponding mean trial-to-trial variance (upper). $[Ca^{2+}]_e$ = 10 mM, $[BayK8644]_e$ = 5μM.

(G) Grand average (lines with filled circles) of variance versus mean relationships (n [Bsn^{wt}] = 27 IHCs, n [$Bsn^{\Delta Ex4/5}$] = 22 IHCs). Filled areas depict SD of grand average of variance. Broken lines represent grand average of parabolic fits (Supplemental Experimental Procedures).

both variance and mean were reduced in $Bsn^{\Delta Ex4/5}$ IHCs (Figures 3F and 3G). The analysis indicated a ~20% decrease in the number of functional Ca^{2+} channels but statistically indistinguishable single-channel currents and maximal open probabilities in the presence of BayK8644 (Table 1 and Table S1). We note that due to uncertainties associated with the channel property estimates from fluctuation analysis (Table 1 and Table S1), which also deviate from those obtained from single-channel recordings in immature IHCs (Zampini et al., 2010), emphasis is on comparison between the genotypes rather than on absolute values (see also Supplemental Experimental Procedures).

Presynaptic Ca^{2+} microdomains, primarily reflecting Ca^{2+} influx at the AZ (Frank et al., 2009), were visualized with the low-affinity Ca^{2+} indicator Fluo-5N (400 μM, K_d = 95 μM) in conjunction with the slow Ca^{2+} chelator EGTA (2 mM). The Ca^{2+} microdomain amplitude (ΔF) measured under these conditions probably reflects a linear summation of the Ca^{2+} influx contributed by the individual presynaptic Ca^{2+} channels (Frank et al., 2009). Consistent with the finding of $Ca_V1.3$ channel clusters in immunohistochemistry, we readily observed Ca^{2+} microdomains also in $Bsn^{\Delta Ex4/5}$ IHCs (Figure 4A). However, their average amplitude (ΔF_{avg}; Table 1), measured at −7 mV in spot-detection experiments at the center of the Ca^{2+} microdomains, was reduced to 36% of control (Figures 4B and 4C), exceeding the reduction of whole-cell I_{Ca} (to 60%–70%; Figure 3) and $Ca_V1.3$ immunofluorescence (to 58%; Figure 2). Augmenting influx through $Ca_V1.3$ Ca^{2+} channels (5 μM BayK8644) alleviated the amplitude reduction of synaptic Ca^{2+} influx in $Bsn^{\Delta Ex4/5}$ IHCs

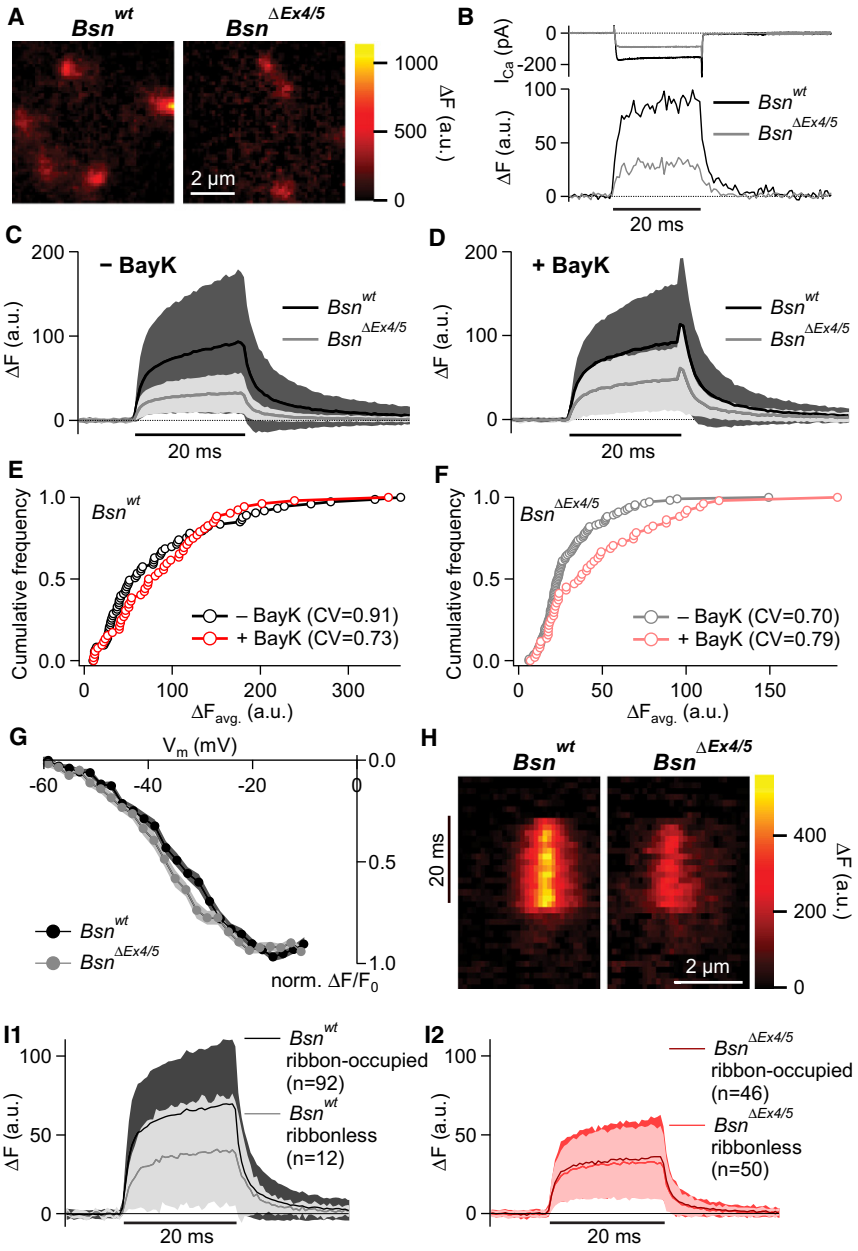

Figure 4. Reduced Presynaptic Ca^{2+} Influx

(A) Exemplary localized Ca^{2+} influx sites in optical sections through the basal part of IHCs (Experimental Procedures). Resting fluorescence (F_0) was subtracted (ΔF images). Ca^{2+} microdomains at AZs are present in $Bsn^{\Delta Ex4/5}$ IHCs, albeit of smaller amplitude.

(B) Exemplary spot-detection responses during depolarization to −7 mV (bar, lower; all reported responses were from the Ca^{2+} microdomain center) and simultaneously acquired whole-cell I_{Ca} (upper). Note the out-of-proportion reduction of presynaptic Ca^{2+} influx.

(C) Grand average of spot-detection responses from Ca^{2+} microdomains (n [Bsn^{wt}] = 74 AZs/30 IHCs, n [$Bsn^{\Delta Ex4/5}$] = 112 AZs/45 IHCs); shaded areas indicate SD.

(D) Same as (C) but in presence of 5 µM BayK8644 (n [Bsn^{wt}] = 53 AZs/21 IHCs, n [$Bsn^{\Delta Ex4/5}$] = 52 AZs/20 IHCs). Note the peak at the end of the stimulation, corresponding to tail current-mediated Ca^{2+} influx (prolonged due to BayK8644).

(E and F) Cumulative frequency distributions of Bsn^{wt} (E) and $Bsn^{\Delta Ex4/5}$ (F) Ca^{2+} microdomain amplitudes (averaged over the second half of the stimulus) in either absence (black/gray) or presence (red/light red) of 5 µM BayK8644. CV denotes coefficient of variation (SD/mean).

(G) Normalized steady-state fluorescence-voltage relationships (n [Bsn^{wt}] = 19 AZs, n [$Bsn^{\Delta Ex4/5}$] = 27 AZs). Relative fluorescence changes were averaged over the last 14.6 ms of the 20 ms stimulus and normalized to the peak response of the given Ca^{2+} microdomain. Shaded areas depict SEM.

(H) Representative line scans across the Ca^{2+} microdomain center (5 mM $[Ca^{2+}]_e$). Bar indicates period of depolarization to −7 mV.

(I) Grand average of Bsn^{wt} (I1) and $Bsn^{\Delta Ex4/5}$ (I2) spot-detection responses, sorted according to the presence/absence of a colocalized ribbon (Experimental Procedures). n (Bsn^{wt}) = 104 AZs/32 IHCs, n ($Bsn^{\Delta Ex4/5}$) = 96 AZs/37 IHCs.

(to 52% of control; Figure 4D and Table 1) and increased amplitude variability among the $Bsn^{\Delta Ex4/5}$, but not the Bsn^{wt} synapses (Figures 4E and 4F). Kinetics (Figures 4C and 4D, Figure S3, and Table S1), voltage dependence (Figure 4G, Figure S3, and Table S1), and spatial extent (Figure 4H and Table S1) of the Ca^{2+} microdomains in $Bsn^{\Delta Ex4/5}$ IHCs were similar to control. There was, however, a tendency toward faster kinetics and more negative activation of $Bsn^{\Delta Ex4/5}$ Ca^{2+} microdomains (Table S1). While the former may reflect differences in Ca^{2+} buffering and/or diffusion, the latter may indicate an altered gating of presynaptic Ca^{2+} channels in the absence of Bassoon and/or the ribbon.

In a second set of experiments, we studied Ca^{2+} signaling at ribbonless and ribbon-occupied AZs in separation with a fluorescent RIBEYE-binding peptide to identify ribbon-occupied AZs (Frank et al., 2009; Zenisek et al., 2004) in both $Bsn^{\Delta Ex4/5}$ and Bsn^{wt} IHCs. While Ca^{2+} microdomains at ribbon-occupied AZs had larger amplitudes than ribbonless synapses in Bsn^{wt} IHCs, there was no significant difference between ribbonless and ribbon-occupied AZs in $Bsn^{\Delta Ex4/5}$ IHCs (Figure 4I). The latter finding was unexpected given their difference in $Ca_V1.3$ immunofluorescence but could reflect limited sensitivity of functional Ca^{2+} imaging, precluding detection of very dim Ca^{2+} signals at $Bsn^{\Delta Ex4/5}$ ribbonless synapses. In summary, the reduced amplitude of Ca^{2+} microdomains and its partial alleviation upon the BayK8644-mediated increase in open probability led us to conclude that $Bsn^{\Delta Ex4/5}$ synapses contain fewer Ca^{2+} channels with a lower open probability.

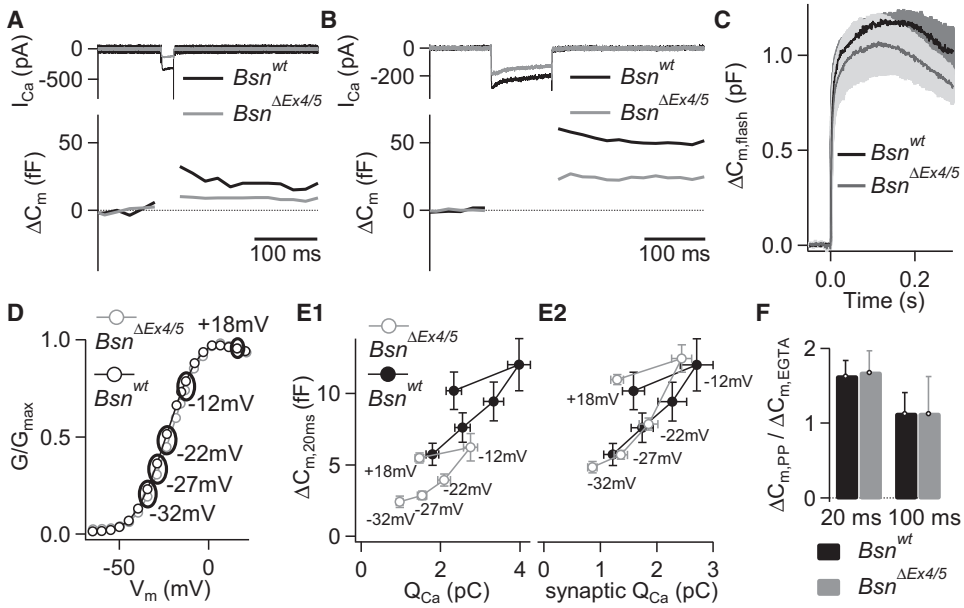

Figure 5. Reduced Exocytosis but Normal Ca^{2+} Influx-Exocytosis Coupling

(A) Representative membrane capacitance changes (ΔC_m) and Ca^{2+} currents (I_{Ca}) in response to 20 ms depolarizations to peak-I_{Ca} V_m.

(B) Same as (A) but in response to 100 ms depolarizations. See Table 1 for pooled data (A and B).

(C) Average ΔC_m responses recorded during flash photolysis of caged Ca^{2+}. Dataset comprises IHCs (n [Bsn^{wt}] = 4, n [$Bsn^{\Delta Ex4/5}$] = 6) with comparable postflash $[Ca^{2+}]_i$, (range: 25–37 μM; Table S1); 0 ms indicates time of UV flash delivery.

(D) Normalized conductance (G)-voltage relationships for both genotypes.

(E1) Summary of exocytic ΔC_m responses to 20 ms depolarizations to the five test potentials depicted in (D) plotted versus the corresponding mean Ca^{2+} current integrals (Q_{Ca}). Pulses were applied to 21 Bsn^{wt} IHCs and 23 $Bsn^{\Delta Ex4/5}$ IHCs in random order at intervals of > 30 s. Note the larger responses at +18 mV compared to −27 mV, despite similar Q_{Ca}, coinciding with a larger p_{open} of Ca^{2+} channels (see D). (E2) To compare the relation between p_{open} and the efficiency of synaptic vesicle release in the two genotypes, we applied three transformations to the plot shown in (E1): (1) assuming a certain extrasynaptic N_{Ca} (Brandt et al., 2005), we estimated the fraction of presynaptic Ca^{2+} channels (out of total N_{Ca}; Table 1), and multiplied Q_{Ca} by the respective ratio (<1) to estimate "synaptic Q_{Ca}." (2) We then doubled the mutant ΔC_m data to account for the halving of membrane-proximal synaptic vesicles seen at mutant AZs (Figure 1). (3) Last, we accounted for the apparently reduced number of presynaptic Ca^{2+} channels at mutant AZs by multiplying mutant Q_{Ca} by 1/0.52 (assuming that the Ca^{2+} microdomain amplitude in the presence of BayK8644 presents the most reliable reflection of presynaptic N_{Ca}; Table 1).

(F) Ratio of exocytic responses (20 ms and 100 ms depolarizations to peak-I_{Ca} V_m) between perforated-patch (endogenous Ca^{2+} buffers) and ruptured-patch ($[EGTA]_i$ = 5 mM) configurations for Bsn^{wt} and $Bsn^{\Delta Ex4/5}$ IHCs (Table 1).

The error bars in (C, D, E, and F) represent SEM.

The reduction of presynaptic Ca^{2+} influx beyond the decrease observed in whole-cell I_{Ca} indicates a higher proportion of extrasynaptic channels in $Bsn^{\Delta Ex4/5}$ IHCs.

Reduced RRP and Sustained Exocytosis but Intact Ca^{2+} Influx-Exocytosis Coupling

How does the reduction of Ca^{2+} channels and membrane-proximal vesicles—as well as a potential mislocalization of these two elements—affect hair cell exocytosis? We addressed this question in $Bsn^{\Delta Ex4/5}$ IHCs by measuring exocytic membrane capacitance changes (ΔC_m) in response to short (20 ms, $\Delta C_{m,\ 20\ ms}$) and longer (100 ms, $\Delta C_{m,\ 100\ ms}$) depolarizations to the maximum Ca^{2+} current potential in native buffering conditions (perforated-patch configuration; Figure 5). Based on previous work (Goutman and Glowatzki, 2007; Li et al., 2009; Meyer et al., 2009; Neef et al., 2009; Rutherford and Roberts, 2006; Schnee et al., 2005), we interpret $\Delta C_{m,\ 20\ ms}$ as fast (synchronous) exocytosis, representing release of a standing RRP, and the difference between $\Delta C_{m,\ 100\ ms}$ and $\Delta C_{m,\ 20\ ms}$ as sustained exocytosis, reflecting vesicle supply to the RRP and subsequent fusion. In this set of experiments, $\Delta C_{m,\ 20\ ms}$ was reduced to 60% (Figure 5A and Table 1) and sustained exocytosis to 56% (Figure 5B and Table 1). These results are consistent with a model in which RRP size and sustained exocytosis rate are related to the number of physical docking and release sites at the AZ (reduction of membrane-proximal vesicles: ~50%, Figure 1J). To test whether the intrinsic Ca^{2+} dependence of exocytosis differed between genotypes, we used flash photolysis of caged Ca^{2+}, but found comparable time constants of the fast component of the $\Delta C_{m,\ flash}$ for elevations of $[Ca^{2+}]_i$ to 25–37 μM ($Bsn^{\Delta Ex4/5}$: 2.4 ± 0.4 ms, mean postflash $[Ca^{2+}]_i$: 29.0 ± 1.9 μM, n = 6 versus Bsn^{wt}: 2.6 ± 1.1 ms, mean postflash $[Ca^{2+}]_i$: 31.5 ± 2.5, n = 4; Figure 5C and Table S1) suggesting an unaltered biochemical Ca^{2+} sensitivity of exocytosis. Notably, despite the lack of ribbons from most synapses in $Bsn^{\Delta Ex4/5}$ IHCs the amplitude of their flash-evoked C_m rise was statistically indistinguishable from Bsn^{wt}.

The observation that the reduction of Ca^{2+}-influx-triggered exocytosis did not exceed the reduction in the number of membrane-proximal and -tethered vesicles (Figure 1) suggests

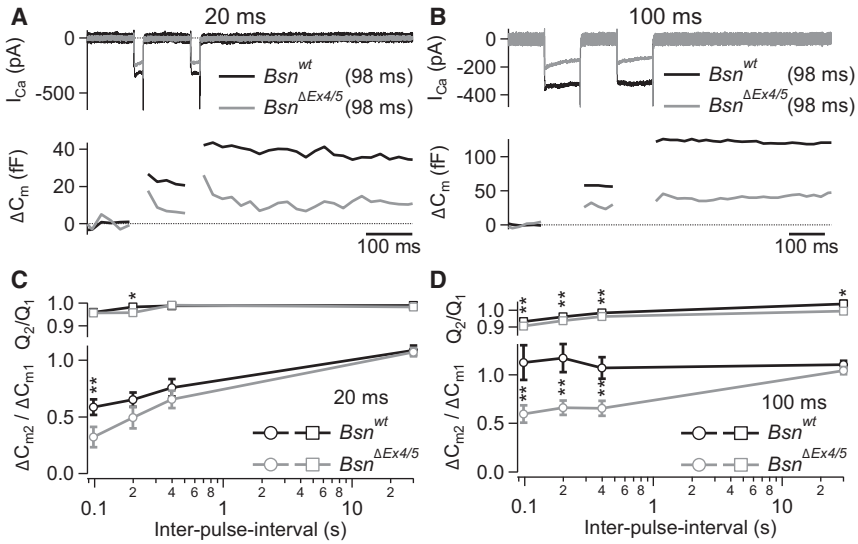

Figure 6. Slowed Vesicle Replenishment Kinetics

(A) Example ΔC_m responses and Ca^{2+} currents (I_{Ca}) from Bsn^{wt} and $Bsn^{\Delta Ex4/5}$ IHCs upon two 20 ms depolarizations to maximum I_{Ca} potential, separated by 98 ms.

(B) Same as (A) but with 100 ms depolarizations.

(C) Summary of paired-pulse ΔC_m recordings following 20 ms depolarizations. The graph shows the ratio of response magnitudes between the second and the first pulse ($\Delta C_{m2}/\Delta C_{m1}$) for different IPIs. Note the depression in both genotypes, which is, however, more pronounced in $Bsn^{\Delta Ex4/5}$ IHCs ($p < 0.01$ for IPI of 98 ms; n [Bsn^{wt}]: 23 to 32 IHCs; n [$Bsn^{\Delta Ex4/5}$]: 20 to 32 IHCs).

(D) Same as (C) but for 100 ms depolarizations. Note the slight facilitation in Bsn^{wt} IHCs but consistent depression in $Bsn^{\Delta Ex4/5}$ IHCs for short IPIs, respectively ($p < 0.01$ for IPI of 98, 198, and 398 ms; n [Bsn^{wt}] = 22 to 35 IHCs; n [$Bsn^{\Delta Ex4/5}$] = 20 to 39 IHCs).

The error bars in (C and D) represent SEM.

that the remaining docking sites are equipped with nearby Ca^{2+} channels (reduction of presynaptic Ca^{2+} channels: ~50%, Table 1; estimated from $Bsn^{\Delta Ex4/5}$ versus Bsn^{wt} presynaptic Ca^{2+} microdomain amplitude in the presence of BayK8644). Yet, a looser coupling between Ca^{2+} channels and vesicle docking sites than implied for the Ca^{2+} nanodomain regime suggested for wild-type IHC AZs could not be excluded (Brandt et al., 2005; Goutman and Glowatzki, 2007; Moser et al., 2006). Therefore, we studied the sensitivity of exocytosis to the slow Ca^{2+} chelator EGTA (Figure 5F). Consistent with the preservation of nanodomain-controlled vesicle fusion in $Bsn^{\Delta Ex4/5}$ IHCs, their $\Delta C_{m,\ 20\ ms}$ in the presence of 5 mM $[EGTA]_i$ was reduced to 58% of control levels (Table 1)—closely resembling the reduction in the presence of endogenous Ca^{2+} buffers (see above). Additionally, we probed RRP exocytosis as a function of Ca^{2+} influx at different membrane potentials (Figures 5D and 5E). Changing the membrane potential manipulates open probability and single-channel current in opposite directions. Thus, exocytosis can be tested for the same absolute Ca^{2+} influx through either few open channels with high single-channel current (mild depolarizations) or more open channels with low single-channel current (strong depolarizations). If exocytosis of a given vesicle was under control of a population of several Ca^{2+} channels (Ca^{2+} microdomain control), exocytosis should be identical for the same Ca^{2+} current independent of the membrane potential. In case of a Ca^{2+} nanodomain control, more exocytosis is expected for more open Ca^{2+} channels, i.e., at more depolarized potentials (hysteresis; Zucker and Fogelson, 1986). This was indeed observed in Bsn^{wt} IHCs (Figure 5E1 and Figure S5), as described before (Brandt et al., 2005), but also in $Bsn^{\Delta Ex4/5}$ IHCs (Figure 5E1 and Figure S5), further arguing that Ca^{2+} nanodomain control of exocytosis is maintained at mutant AZs. As a further consistency check, we scaled the exocytosis-Ca^{2+} current integral relationship of $Bsn^{\Delta Ex4/5}$ IHCs by experimentally derived factors to normalize the data to the lower number of membrane-proximal vesicles and presynaptic Ca^{2+} channels. This resulted largely in an overlap with the wild-type data (Figure 5E2). In summary, the data indicate that the coupling of Ca^{2+} channels to release sites remains intact despite Bassoon disruption but that the rates of initial and sustained exocytosis are reduced to a similar extent as the number of membrane-proximal vesicles.

In Vitro and In Vivo Analysis of Synaptic Vesicle Replenishment

Traditionally, the synaptic ribbon has been assigned a conveyor belt and/or attractor function (Holt et al., 2004; Sterling and Matthews, 2005), according to which it is responsible for rapid supply of vesicles to the RRP and enables high rates of tonic neurotransmitter release (Gomis et al., 1999; Johnson et al., 2008; Moser and Beutner, 2000; Rutherford and Roberts, 2006; Schnee et al., 2005; Spassova et al., 2004). Hence, we tested whether the rate of RRP refilling was reduced in the absence of the ribbon and functional Bassoon protein. Here, we explored vesicle replenishment in vitro by measuring relative ΔC_m in paired-pulse protocols, with the stimuli (20 ms or 100 ms long depolarizations) being separated by various time intervals (98, 198, and 398 ms; Figure 6). The ratio of Ca^{2+} current integrals was close to one in both genotypes (marginally smaller in $Bsn^{\Delta Ex4/5}$ IHCs; Figures 6C and 6D and Table S1) indicating that the Ca^{2+} signals that drive exocytosis were mostly comparable between both pulses. For 20 ms stimuli at short inter-pulse-intervals (IPI: 98 ms) we observed stronger depression of the exocytic response in $Bsn^{\Delta Ex4/5}$ IHCs, indicating a slower recovery of the RRP at $Bsn^{\Delta Ex4/5}$ synapses ($p < 0.01$). For longer recovery times (IPI: 198, 398 ms), the difference did not reach statistical significance. While both Bsn^{wt} and $Bsn^{\Delta Ex4/5}$ IHCs showed depression for short stimuli, Bsn^{wt} IHCs exhibited a tendency toward facilitation for long depolarizations (100 ms). In contrast, $Bsn^{\Delta Ex4/5}$ IHCs also showed depression when challenged with long stimuli ($p < 0.01$ for 98, 198, and 398 ms IPI).

In vivo, we measured the recovery of the auditory nerve fiber response following a masking sound as a proxy of the recovery

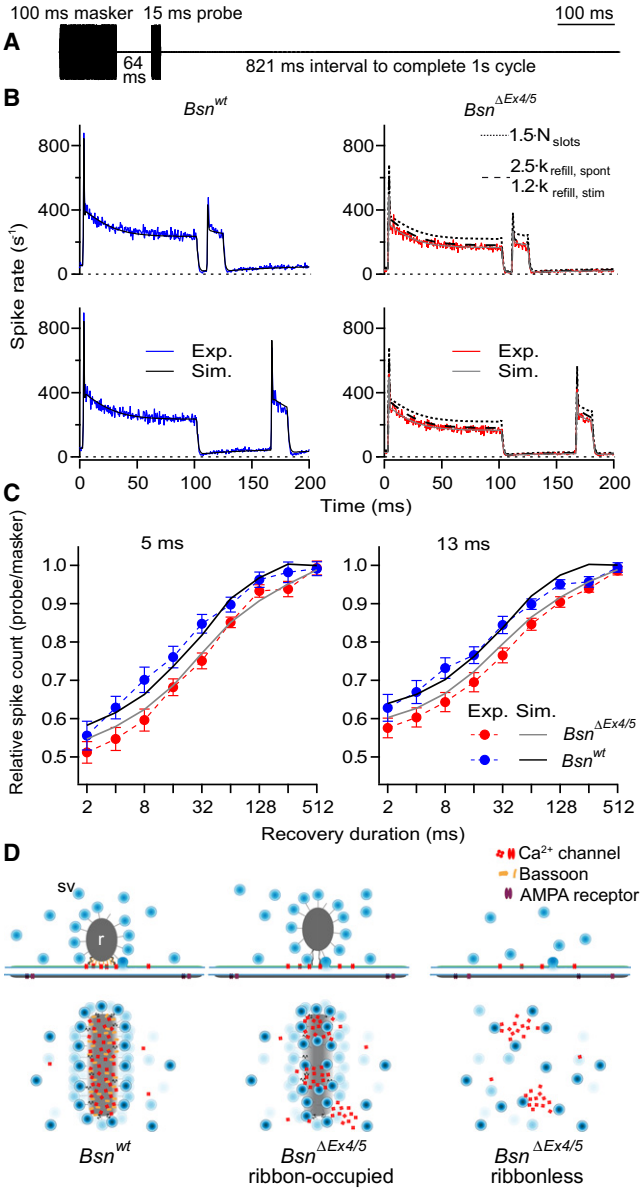

Figure 7. Comparison of Sound-Evoked Spike Rates In Vivo for *Bsn*^{wt} and *Bsn*$^{\Delta Ex4/5}$ Mice

Reduced in vivo action potential rates and minimally enhanced forward masking in auditory nerve fibers can be explained by a vesicle pool model combined with spike refractoriness.

(A) Illustration of the stimulus design: a 100 ms tone burst (masker) is separated from a 15 ms probe stimulus by a silent interval ranging between 2 and 512 ms (example: 64 ms). Both stimuli were presented at characteristic frequency, 30 dB above threshold and with 2.5 ms rise-fall times. The interval between two maskers was always 1 s. Each interval was repeated at least 50 times.

(B) Experimental results (blue [*Bsn*^{wt}], and red [*Bsn*$^{\Delta Ex4/5}$]) and model-predicted (black) spike rates for recovery periods of 8 (upper) and 64 (lower) ms in *Bsn*^{wt} (left, n = 15) and *Bsn*$^{\Delta Ex4/5}$ (right, n = 7) auditory nerve fibers. Dotted line shows the prediction of a model with the set of *Bsn*$^{\Delta Ex4/5}$parameters except *Bsn*^{wt} release site number. Dashed line, instead, results from using *Bsn*$^{\Delta Ex4/5}$parameters with *Bsn*^{wt} vesicle replenishment kinetics.

(C) Experimental (dashed line, symbols representing means ± SEM) and model-predicted (line) relative spike counts during the first 5 (left) and the first 13 (right) ms of the auditory nerve fiber response to the probe stimulus normalized to the response to the masker stimulus. The error bars represent SEM.

(D) Schematic representation of tentative active zone structure at wild-type, ribbon-occupied *Bsn* mutant, and ribbonless *Bsn* mutant afferent IHC synapses, respectively. (Top) Sections; (bottom) view as seen from the synaptic cleft. The illustration summarizes the findings of smaller $Ca_V1.3$ channel/membrane-proximal vesicle complements in the absence of a synaptic ribbon, altered substructure of $Ca_V1.3$ clusters in *Bsn* mutants.

of the presynaptic RRP (Spassova et al., 2004). We used a forward masking paradigm (Harris and Dallos, 1979; Spassova et al., 2004) in which a 100 ms masking stimulus was separated from a 15 ms probe stimulus by a variable silent interval ranging between 2 and 512 ms (Figure 7A). Onset spike rates and adapted spike rates in response to the masking stimulus were reduced by a factor of 1.7 and 1.4, respectively, in *Bsn*$^{\Delta Ex4/5}$ (poststimulus time histograms [PSTHs]; Figure 7B). We found an enhanced forward masking effect in *Bsn*$^{\Delta Ex4/5}$ fibers when comparing each probe response to its masker response (lower ratio of spike rate for probe over spike rate for masker [averaged over the first 5 ms of the probe and the masker] at 4-32 ms interval for mutants, $p < 0.05$ each). There was also a trend toward longer time of half-recovery from masking in *Bsn*$^{\Delta Ex4/5}$ (34.9 ± 5.0 ms in mutant and 23.3 ± 4.9 ms in wild-type, $p = 0.13$).

Taken together, the in vitro and in vivo results suggest a disturbed replenishment of fusion-competent synaptic vesicles in *Bsn*$^{\Delta Ex4/5}$ IHCs. To what degree is the impaired sound coding phenotype in *Bsn*$^{\Delta Ex4/5}$ IHCs caused by a reduction in the number of release sites or by their deficient refilling? To answer this question, we quantified the forward masking data by a model of sound-dependent RRP fusion and replenishment combined with auditory nerve fiber refractoriness. The core parameters of this model are the number of release sites, sound-dependent rates (fusion rate constants and refilling rate constants per release site in the presence and absence of sound), and absolute and relative refractory periods (Supplemental Experimental Procedures). As those parameters are biophysically accessible quantities, the model can be used for quantitative, mechanistic data analysis of auditory nerve fiber responses in the context of cellular physiology.

A single set of parameters accurately reproduced PSTHs for all nine recovery periods (Figure 7B and Figure S6). The very same set of parameters also predicted the ratio of spike counts (probe/masker) for analysis windows of 5 ms and 13 ms following sound onset (Figure 7C). Importantly, the dominating difference between the parameter sets for the two genotypes was a 35% reduction in release site number for *Bsn*$^{\Delta Ex4/5}$ (i.e., the maximal capacity of the RRP; see dotted line in Figure 7B for a simulation with wild-type release site number), while the fusion rates and vesicular release probability remained virtually unchanged (Table S2; consistent with capacitance measurements; Figure 5). Additionally, refilling rate constants were slightly reduced. When assuming wild-type vesicle replenishment kinetics for *Bsn*$^{\Delta Ex4/5}$ fibers—while keeping all other model parameters for this genotype—the adapted spike rates were accordingly slightly improved (see dashed line in Figure 7B).

In summary, using the model as a quantification of the in vivo results allowed us to draw conclusions about presynaptic quantities from postsynaptic measurements. Generally, the model

validated our structural and functional findings, made independently in vitro. Additionally, it advanced our mechanistic understanding by permitting the discrimination between a reduction in the number of (1) generally available release sites and the reduction in the (2) occupancy of those release sites: the parameters suggest that the reduced response amplitude in $Bsn^{\Delta Ex4/5}$ fibers is primarily due to a reduction in the total number of release sites (35%) and to a lesser degree caused by a reduction in their occupancy. These two effects combine such that in the model the number of release sites occupied at rest is reduced to 50% of wild-type, which is in agreement with the 55% reduction in number of membrane-proximal vesicles observed in electron micrographs of $Bsn^{\Delta Ex4/5}$ AZs (Figure 1J).

DISCUSSION

In this study, we examined effects of genetic Bassoon disruption at several structural and functional levels. EM tomography revealed a spectrum of synapse morphologies from wild-type-like to loosely anchored ribbons to ribbonless. Intriguingly, we found that *Bsn* mutant synapses with a partially anchored ribbon (ribbon-occupied) exhibited an intermediate phenotype between wild-type AZs and mutant ribbonless AZs. While fewest presynaptic Ca^{2+} channels were found at ribbonless AZs in $Bsn^{\Delta Ex4/5}$ IHCs, the ribbon-occupied $Bsn^{\Delta Ex4/5}$ AZs harbored more, but still fewer, Ca^{2+} channels than wild-type AZs—similar to the quantification of membrane-proximal vesicles. Fast and sustained exocytosis was reduced in proportion to the overall reduction in membrane-proximal vesicles and Ca^{2+} channels, while the Ca^{2+} sensitivity of exocytosis remained normal. Moreover, vesicle replenishment was impaired. A mechanistic computational model of synaptic transfer, used to fit the in vivo data, independently supported morphological and functional in vitro findings. We conclude that Bassoon disruption and the associated ribbon loss reduces the number of functional release sites, impairs their refilling, and consequently lowers the RRP.

Structural Consequences of Bassoon Disruption and Ribbon Loss

The most prominent phenotype of Bassoon disruption is the loss of synaptic ribbons from a majority of AZs (Khimich et al., 2005; tom Dieck et al., 2005). In contrast to retinal photoreceptors (Specht et al., 2007), mature hair cells of *Bsn* mutants exhibited some (although few) ribbon-occupied synapses at typical locations (Figures 1 and 2). Together with observations at Bsn^{wt} synapses without a ribbon, study of these ribbon-occupied mutant synapses helped to test the role of the synaptic ribbon. Both semiquantitative immunofluorescence microscopy (Figures 2B and 2C) and confocal imaging of presynaptic Ca^{2+} influx (Figure 4I1) revealed that ribbon presence was associated with an increase in the number of Ca^{2+} channels at Bsn^{wt} AZs. Using STED microscopy, we furthermore observed a stripe-like arrangement of the Ca^{2+} channel cluster(s) at ribbon-occupied Bsn^{wt} AZs. These structures were reminiscent of the electron-dense material seen in electron tomograms of AZs in mouse IHCs (Figures 1E2–1H2) and frog saccular hair cells (Lenzi et al., 2002), and the row-like arrays of intramembrane particles observed in freeze-fracture electron micrographs (Roberts et al., 1990; Saito and Hama, 1984). At all $Bsn^{\Delta Ex4/5}$ synapses, this $Ca_V1.3$ cluster geometry was dissolved into a pattern of small spots (Figure 2F), similar to alterations of presynaptic densities seen in electron tomography (Figures 1E2–1G2). This coincidence supports the view that the $Ca_V1.3$ clusters are an integral part of the presynaptic density (Lenzi et al., 2002). While this difference in cluster geometry could, in principle, reflect a direct effect of Bassoon loss, we did not find evidence for direct interactions between Bassoon and $Ca_V1.3$ (heterologous expression; Figure S4). The observation of spots rather than stripes at ribbon-occupied $Bsn^{\Delta Ex4/5}$ synapses might also reflect a decreased organizational impact of the ribbon when its anchorage is loosened. It is interesting to note that the CAST/ELKS1 homolog Bruchpilot has been implicated in clustering of presynaptic Ca^{2+} channels at the *Drosophila* neuromuscular junction (Kittel et al., 2006). Bruchpilot is an integral component of presynaptic electron-dense projections (T-bars, which were absent in *Bruchpilot* mutants) and physically interacts with presynaptic Ca^{2+} channels, at least in vitro (Fouquet et al., 2009).

Our finding of abnormal clustering of presynaptic Ca^{2+} channels upon Bassoon disruption is supported by a comparison between the associated reduction in whole-cell (~20%) and presynaptic Ca^{2+} influx (~50%; both in the presence of BayK8644). The stronger decrease in presynaptic Ca^{2+} influx indicates an increased fraction of extrasynaptic Ca^{2+} channels in mutant IHCs. Similar to Ca^{2+} channels, the number of membrane-proximal vesicles appears to be greater when the ribbon is present. At least by trend, ribbonless mutant AZs showed the fewest vesicles, whereas the presence of a ribbon increased this figure, but not to wild-type levels.

Functional Consequences of Bassoon Disruption and Ribbon Loss

How do these findings relate to synaptic function? Specifically, how are the number of release sites—formed by vesicle docking sites and closely colocalized Ca^{2+} channels—and synaptic exocytosis affected by Bassoon disruption? First, when probing fast and sustained exocytosis in $Bsn^{\Delta Ex4/5}$ IHCs, we observed a decrease in amplitude that was roughly comparable to the observed reduction in vesicle number and presynaptic Ca^{2+} channel number. Second, both intrinsic and apparent Ca^{2+} cooperativity of exocytosis was normal in $Bsn^{\Delta Ex4/5}$ IHCs. Together, these observations suggest that the coupling between Ca^{2+} influx through the remaining Ca^{2+} channels and the fusion of the remaining vesicles was unaffected. Yet one faces the caveat that a static technique such as EM cannot distinguish between fewer physical docking sites or their lower occupancy due to impaired replenishment. Thus, distinguishing between these two scenarios is aided by probing vesicle resupply, which was slightly impaired in $Bsn^{\Delta Ex4/5}$ mice (Figure 6). This finding stands in agreement with the study of Hallermann and colleagues (Hallermann et al., 2010), which shows that vesicle reloading at a central synapse is impaired in *Bsn* mutants, evident by enhanced synaptic depression during sustained high-frequency trains. However, our study of a ribbon synapse revealed additional defects; fitting a mechanistic computational model to our in vivo data (Figure 7 and Figure S6) indicated that synaptic transmission at the IHC synapse of $Bsn^{\Delta Ex4/5}$ was

impaired primarily due to a reduced number of functional release sites (in accordance with our morphological and functional in vitro data) and, to a lesser extent, their slower refilling under the given stimulus protocol (Figure 7).

Toward Disentangling the Interplay between Bassoon and the Synaptic Ribbon

Bassoon, via interaction with RIBEYE (tom Dieck et al., 2005), contributes to ribbon anchorage. In hair cells, some residual and partial ribbon anchorage is observed, probably involving additional anchoring proteins. Those ribbon-occupied *Bsn* mutant synapses were inferior to their wild-type counterparts with regard to both Ca^{2+} channel clustering and membrane tethering of vesicles. These observations could either be explained by (1) a direct effect of functional Bassoon loss, or (2) by a limited capacity of those "sick ribbons" ribbons to perform their task(s). Several recent studies at "conventional" synapses show that Bassoon is not required for synaptic transmission per se but is involved in clustering (Mukherjee et al., 2010) and replenishment of synaptic vesicles (Hallermann et al., 2010). Our results are generally consistent with these findings; however, ribbon synapses do require Bassoon also for basic synaptic transmission. It is likely that the more severe synaptic phenotype found in IHCs reflects the perturbation of ribbon-supported functions. For example, in contrast to Hallermann et al. (2010), we do find a substantial reduction in the number of release sites in *Bsn* mutant IHCs. Additionally, the trend toward fewer membrane-tethered vesicles in general but more vesicles at ribbon-occupied than ribbonless *Bsn* mutant synapses could, for example, be explained by a combinatorial effect of primary Bassoon loss and secondary Piccolo loss (Mukherjee et al., 2010) in the case of ribbonless synapses. Interestingly, no evidence for a reduced quantal content was found in *Bsn* mutant cerebellar synapses by Hallermann et al. (2010). However, the complex nature of interactions between the numerous members of the cytomatrix of the active zone (Schoch and Gundelfinger, 2006) demand careful evaluation of "one-protein, one-function" hypotheses. The absence of detectable direct effects of Bassoon disruption on basal synaptic transmission at conventional synapses (Hallermann et al., 2010; Mukherjee et al., 2010) and the intermediate phenotypes seen in ribbon-occupied mutant synapses might favor a hypothesis of "sick ribbons" over direct Bassoon effects underlying the majority of observed synaptic and auditory phenotypes in *Bsn* mutants. Future studies, including silencing of ribbon components such as Piccolo and RIBEYE, are required to further our understanding of the roles of the synaptic ribbon and Bassoon for active zone structure and function as well as their dynamic regulation.

EXPERIMENTAL PROCEDURES

A more detailed version of the Experimental Procedures is published in Supplemental Information. Unless stated otherwise, all chemicals were obtained from Sigma-Aldrich.

Animals

Mice with deletion of exons 4 and 5 of the Bassoon gene ($Bsn^{\Delta Ex4/5}$; Altrock et al., 2003) or carrying a gene-trapped allele (Bsn^{gt}, Lexicon Pharmaceuticals, Inc.), and wild-type littermates were used. All experiments were approved by the University of Göttingen Board for Animal Welfare and the Animal Welfare Office of the State of Lower Saxony.

Immunohistochemistry

Apical cochlear turns were fixed in methanol for 20 min at −20°C and prepared as previously described (Khimich et al., 2005; Meyer et al., 2009). The following antibodies were used: mouse anti-CtBP2 (BD Biosciences), rabbit anti-GluR2/3 (Chemicon), rabbit anti-$Ca_V1.3$ (Alomone Labs), mouse anti-GluR2 (Chemicon), mouse anti-Sap7f407 to Bassoon (Abcam), and rabbit anti-BSN1.6 to Bassoon (provided by E.D. Gundelfinger).

Confocal and STED Microscopy

Confocal image stacks were acquired with a Leica SP5 microscope and 100× oil immersion objective. For STED-imaging, two different microscopes were used: the Leica TCS STED (Figures 2D and 2E) and a custom apparatus (Harke et al., 2008) with a resolution of around 80 nm. For size and shape analysis of Ca^{2+} channel clusters, XY scans were acquired after finding the fluorescence maximum with a XZ-scan.

Electron Microscopy and Tomography

Cochleae were processed for electron microscopy as described (Meyer et al., 2009 and Pangršič et al., 2010). Thin sections were examined with a Philips CM120 BioTwin transmission electron microscope (Philips Inc.) with a TemCam F224A camera (TVIPS) at 20,000× magnification. Images were subsequently analyzed with iTEM software (Olympus). Tilt series from 250 nm sections were recorded at 27,500× magnification in the range of 129°, then calculated with Etomo (http://bio3d.colorado.edu/).

Patch-Clamp and Confocal Ca^{2+} Imaging of IHCs

IHCs from apical coils of freshly dissected organs of Corti (P20 through P31) were patch-clamped as described (Moser and Beutner, 2000) and fluctuation analysis (FA) was performed similarly as previously described (Meyer et al., 2009). Currents were low-pass filtered at 8.5 kHz or 5 kHz and sampled at 100 kHz (FA) or 40 kHz (Ca^{2+} currents, ΔC_m measurements), respectively. Cells with holding current > −50 pA were discarded. Ca^{2+} currents were further isolated with a P/n protocol. In FA and Ca^{2+} current activation recordings, series resistance was compensated online (20%–50%; τ = 10 μs). Residual series resistance averaged 4.4 ± 0.4 MΩ (Bsn^{wt}; n = 35 ensembles) and 4.3 ± 0.3 MΩ ($Bsn^{\Delta Ex4/5}$; n = 33 ensembles) in FA experiments. Flash photolysis was performed essentially as described in Beutner et al. (2001). Confocal Ca^{2+} imaging was performed as described (Frank et al., 2009).

Single-Unit Recordings

Single-unit recordings from auditory nerve fibers of 6- to 10–week-old Bsn^{wt} and $Bsn^{\Delta Ex4/5}$ mice (n = 7 each) were performed as described by Taberner and Liberman (2005) and Buran et al. (2010).

Data Analysis

Data analysis was performed with Matlab (Mathworks), Igor Pro (Wavemetrics), and ImageJ software and is described in more detail in Supplemental Information. Two-tailed t tests or the Mann-Whitney-Wilcoxon test were used for statistical comparisons between two samples (*$p < 0.05$, **$p < 0.01$, ***$p < 0.001$).

SUPPLEMENTAL INFORMATION

Supplemental Information includes Supplemental Experimental Procedures, six figures, two tables, and two movies and can be found with this article online at doi:10.1016/j.neuron.2010.10.027.

ACKNOWLEDGMENTS

We thank S. Blume, N. Dankenbrink-Werder, A. Gonzalez, M. Köppler, and B. Kracht for expert technical assistance. This work was supported by grants of the Max Planck Society (Tandem-Project grant to Nils Brose and T.M.), the German Research Foundation Fellowship to N.S., Center for Molecular

Physiology of the Brain Grant FZT-103 to T.M. and A.E., the German Federal Ministry of Education and Research (01GQ0810, Bernstein Focus for Neurotechnology) to T.M. and A.E., the State of Saxony-Anhalt/European Structural Funds (EFRE-IfN C2/1) to E.D.G., and by the National Institutes of Health (Grants DC0188 to M.C.L., DC009433 and HL087120 to A.L., and T32 AI 07260 to K.E.B.). M.A.R. and T.P. were supported by fellowships of the Alexander von Humboldt Foundation. A.N. is a Fellow of the Bernstein Center for Computational Neuroscience Göttingen. The study was designed by T.M., T.F., N.S., A.N., and D.R. The experimental work was performed by T.F. (Ca^{2+} imaging, Ca^{2+} current, and C_m recordings), M.A.R. (confocal and STED microscopy), N.S. (single-unit recordings under supervision of M.C.L.), T.P. (flash photolysis), D.K. (confocal microscopy), and D.R. (electron microscopy). A.E. and B.H. contributed to STED microscopy, and A.E. contributed to image analysis. A.N. performed modeling and contributed to data analysis. A.F. and E.D.G. provided the mice (gene trap mutant in collaboration with Lexicon Pharmaceuticals) and discussion. K.E.B and A.L. performed protein-protein interaction experiments. T.M., T.F., N.S., A.N., and M.A.R. prepared the manuscript.

Accepted: October 8, 2010
Published: November 17, 2010

REFERENCES

Altrock, W.D., tom Dieck, S., Sokolov, M., Meyer, A.C., Sigler, A., Brakebusch, C., Fässler, R., Richter, K., Boeckers, T.M., Potschka, H., et al. (2003). Functional inactivation of a fraction of excitatory synapses in mice deficient for the active zone protein bassoon. Neuron *37*, 787–800.

Beutner, D., Voets, T., Neher, E., and Moser, T. (2001). Calcium dependence of exocytosis and endocytosis at the cochlear inner hair cell afferent synapse. Neuron *29*, 681–690.

Brandt, A., Khimich, D., and Moser, T. (2005). Few CaV1.3 channels regulate the exocytosis of a synaptic vesicle at the hair cell ribbon synapse. J. Neurosci. *25*, 11577–11585.

Buran, B.N., Strenzke, N., Neef, A., Gundelfinger, E.D., Moser, T., and Liberman, M.C. (2010). Onset coding is degraded in auditory nerve fibers from mutant mice lacking synaptic ribbons. J. Neurosci. *30*, 7587–7597.

Dick, O., Hack, I., Altrock, W.D., Garner, C.C., Gundelfinger, E.D., and Brandstätter, J.H. (2001). Localization of the presynaptic cytomatrix protein Piccolo at ribbon and conventional synapses in the rat retina: Comparison with Bassoon. J. Comp. Neurol. *439*, 224–234.

Dick, O., tom Dieck, S., Altrock, W.D., Ammermüller, J., Weiler, R., Garner, C.C., Gundelfinger, E.D., and Brandstätter, J.H. (2003). The presynaptic active zone protein bassoon is essential for photoreceptor ribbon synapse formation in the retina. Neuron *37*, 775–786.

Fernández-Busnadiego, R., Zuber, B., Maurer, U.E., Cyrklaff, M., Baumeister, W., and Lucic, V. (2010). Quantitative analysis of the native presynaptic cytomatrix by cryoelectron tomography. J. Cell Biol. *188*, 145–156.

Fouquet, W., Owald, D., Wichmann, C., Mertel, S., Depner, H., Dyba, M., Hallermann, S., Kittel, R.J., Eimer, S., and Sigrist, S.J. (2009). Maturation of active zone assembly by Drosophila Bruchpilot. J. Cell Biol. *186*, 129–145.

Frank, T., Khimich, D., Neef, A., and Moser, T. (2009). Mechanisms contributing to synaptic Ca2+ signals and their heterogeneity in hair cells. Proc. Natl. Acad. Sci. USA *106*, 4483–4488.

Furukawa, T., and Matsuura, S. (1978). Adaptive rundown of excitatory postsynaptic potentials at synapses between hair cells and eight nerve fibres in the goldfish. J. Physiol. *276*, 193–209.

Glowatzki, E., Grant, L., and Fuchs, P. (2008). Hair cell afferent synapses. Curr. Opin. Neurobiol. *18*, 389–395.

Gomis, A., Burrone, J., and Lagnado, L. (1999). Two actions of calcium regulate the supply of releasable vesicles at the ribbon synapse of retinal bipolar cells. J. Neurosci. *19*, 6309–6317.

Goutman, J.D., and Glowatzki, E. (2007). Time course and calcium dependence of transmitter release at a single ribbon synapse. Proc. Natl. Acad. Sci. USA *104*, 16341–16346.

Hallermann, S., Fejtova, A., Schmidt, H., Weyhersmüller, A., Silver, R.A., Gundelfinger, E.D., and Eilers, J. (2010). Bassoon speeds vesicle recruitment at a central excitatory synapse. Neuron *68*, this issue, 710–723.

Harke, B., Keller, J., Ullal, C.K., Westphal, V., Schönle, A., and Hell, S.W. (2008). Resolution scaling in STED microscopy. Opt. Express *16*, 4154–4162.

Harris, D.M., and Dallos, P. (1979). Forward masking of auditory nerve fiber responses. J. Neurophysiol. *42*, 1083–1107.

Holt, M., Cooke, A., Neef, A., and Lagnado, L. (2004). High mobility of vesicles supports continuous exocytosis at a ribbon synapse. Curr. Biol. *14*, 173–183.

Johnson, S.L., Forge, A., Knipper, M., Münkner, S., and Marcotti, W. (2008). Tonotopic variation in the calcium dependence of neurotransmitter release and vesicle pool replenishment at mammalian auditory ribbon synapses. J. Neurosci. *28*, 7670–7678.

Khimich, D., Nouvian, R., Pujol, R., tom Dieck, S., Egner, A., Gundelfinger, E.D., and Moser, T. (2005). Hair cell synaptic ribbons are essential for synchronous auditory signalling. Nature *434*, 889–894.

Kittel, R.J., Wichmann, C., Rasse, T.M., Fouquet, W., Schmidt, M., Schmid, A., Wagh, D.A., Pawlu, C., Kellner, R.R., Willig, K.I., et al. (2006). Bruchpilot promotes active zone assembly, Ca2+ channel clustering, and vesicle release. Science *312*, 1051–1054.

Lenzi, D., Crum, J., Ellisman, M.H., and Roberts, W.M. (2002). Depolarization redistributes synaptic membrane and creates a gradient of vesicles on the synaptic body at a ribbon synapse. Neuron *36*, 649–659.

Li, G.L., Keen, E., Andor-Ardó, D., Hudspeth, A.J., and von Gersdorff, H. (2009). The unitary event underlying multiquantal EPSCs at a hair cell's ribbon synapse. J. Neurosci. *29*, 7558–7568.

Meyer, A.C., Frank, T., Khimich, D., Hoch, G., Riedel, D., Chapochnikov, N.M., Yarin, Y.M., Harke, B., Hell, S.W., Egner, A., and Moser, T. (2009). Tuning of synapse number, structure and function in the cochlea. Nat. Neurosci. *12*, 444–453.

Moser, T., and Beutner, D. (2000). Kinetics of exocytosis and endocytosis at the cochlear inner hair cell afferent synapse of the mouse. Proc. Natl. Acad. Sci. USA *97*, 883–888.

Moser, T., Neef, A., and Khimich, D. (2006). Mechanisms underlying the temporal precision of sound coding at the inner hair cell ribbon synapse. J. Physiol. *576*, 55–62.

Mukherjee, K., Yang, X., Gerber, S.H., Kwon, H.B., Ho, A., Castillo, P.E., Liu, X., and Südhof, T.C. (2010). Piccolo and bassoon maintain synaptic vesicle clustering without directly participating in vesicle exocytosis. Proc. Natl. Acad. Sci. USA *107*, 6504–6509.

Neef, J., Gehrt, A., Bulankina, A.V., Meyer, A.C., Riedel, D., Gregg, R.G., Strenzke, N., and Moser, T. (2009). The Ca2+ channel subunit beta2 regulates Ca2+ channel abundance and function in inner hair cells and is required for hearing. J. Neurosci. *29*, 10730–10740.

Neher, E., and Sakaba, T. (2008). Multiple roles of calcium ions in the regulation of neurotransmitter release. Neuron *59*, 861–872.

Nouvian, R., Beutner, D., Parsons, T.D., and Moser, T. (2006). Structure and function of the hair cell ribbon synapse. J. Membr. Biol. *209*, 153–165.

Pangršič, T., Lasarow, L., Reuter, K., Takago, H., Schwander, M., Riedel, D., Frank, T., Tarantino, L.M., Bailey, J.S., Strenzke, N., et al. (2010). Hearing requires otoferlin-dependent efficient replenishment of synaptic vesicles in hair cells. Nat. Neurosci. *13*, 869–876.

Pauli-Magnus, D., Hoch, G., Strenzke, N., Anderson, S., Jentsch, T.J., and Moser, T. (2007). Detection and differentiation of sensorineural hearing loss in mice using auditory steady-state responses and transient auditory brainstem responses. Neuroscience *149*, 673–684.

Roberts, W.M., Jacobs, R.A., and Hudspeth, A.J. (1990). Colocalization of ion channels involved in frequency selectivity and synaptic transmission at presynaptic active zones of hair cells. J. Neurosci. *10*, 3664–3684.

Rutherford, M.A., and Roberts, W.M. (2006). Frequency selectivity of synaptic exocytosis in frog saccular hair cells. Proc. Natl. Acad. Sci. USA *103*, 2898–2903.

Saito, K., and Hama, K. (1984). A freeze-fracture study of afferent and efferent synapses of hair cells in the sensory epithelium of the organ of Corti in the guinea pig. Cell Tissue Res. *238*, 437–446.

Schmitz, F., Königstorfer, A., and Südhof, T.C. (2000). RIBEYE, a component of synaptic ribbons: A protein's journey through evolution provides insight into synaptic ribbon function. Neuron *28*, 857–872.

Schnee, M.E., Lawton, D.M., Furness, D.N., Benke, T.A., and Ricci, A.J. (2005). Auditory hair cell-afferent fiber synapses are specialized to operate at their best frequencies. Neuron *47*, 243–254.

Schoch, S., and Gundelfinger, E.D. (2006). Molecular organization of the presynaptic active zone. Cell Tissue Res. *326*, 379–391.

Spassova, M.A., Avissar, M., Furman, A.C., Crumling, M.A., Saunders, J.C., and Parsons, T.D. (2004). Evidence that rapid vesicle replenishment of the synaptic ribbon mediates recovery from short-term adaptation at the hair cell afferent synapse. J. Assoc. Res. Otolaryngol. *5*, 376–390.

Specht, D., tom Dieck, S., Ammermüller, J., Regus-Leidig, H., Gundelfinger, E.D., and Brandstätter, J.H. (2007). Structural and functional remodeling in the retina of a mouse with a photoreceptor synaptopathy: Plasticity in the rod and degeneration in the cone system. Eur. J. Neurosci. *26*, 2506–2515.

Sterling, P., and Matthews, G. (2005). Structure and function of ribbon synapses. Trends Neurosci. *28*, 20–29.

Taberner, A.M., and Liberman, M.C. (2005). Response properties of single auditory nerve fibers in the mouse. J. Neurophysiol. *93*, 557–569.

tom Dieck, S., Altrock, W.D., Kessels, M.M., Qualmann, B., Regus, H., Brauner, D., Fejtová, A., Bracko, O., Gundelfinger, E.D., and Brandstätter, J.H. (2005). Molecular dissection of the photoreceptor ribbon synapse: Physical interaction of Bassoon and RIBEYE is essential for the assembly of the ribbon complex. J. Cell Biol. *168*, 825–836.

Wittig, J.H., Jr., and Parsons, T.D. (2008). Synaptic ribbon enables temporal precision of hair cell afferent synapse by increasing the number of readily releasable vesicles: A modeling study. J. Neurophysiol. *100*, 1724–1739.

Zampini, V., Johnson, S.L., Franz, C., Lawrence, N.D., Münkner, S., Engel, J., Knipper, M., Magistretti, J., Masetto, S., and Marcotti, W. (2010). Elementary properties of CaV1.3 Ca(2+) channels expressed in mouse cochlear inner hair cells. J. Physiol. *588*, 187–199.

Zenisek, D., Horst, N.K., Merrifield, C., Sterling, P., and Matthews, G. (2004). Visualizing synaptic ribbons in the living cell. J. Neurosci. *24*, 9752–9759.

Zucker, R.S., and Fogelson, A.L. (1986). Relationship between transmitter release and presynaptic calcium influx when calcium enters through discrete channels. Proc. Natl. Acad. Sci. USA *83*, 3032–3036.